High Cell to Module Efficiency Remaining Ratio of ≈90% for the 100 cm^2 Fully Roll-to-Roll Gravure Printed Flexible Organic Solar Cells From Non-Halogenated Solvent

Shutao Yang, Xingze Chen, Yaqin Pan, Jin Fang, Yunfei Han, Zhenguo Wang, Fan Qian, Weitao Qi, Ke Shui, Qing Zhang, Fengqi Guo, Yanming Sun,* Chang-Qi Ma,* and Qun Luo**

The cell-to-module (CTM) efficiency remaining ratio from monolithic device to large-area module indicates the scalability potential for large-area organic solar cells (OSCs). Nowadays, the CTM value is still low as the area increases to larger than 100 cm^2. In this work, the crucial role of solvent in CTM for printing, which on one side influenced the large area homogeneity due to the ink rheology property, and on the other side impacted phase separation dynamics because of vaporization and crystalline rate is highlighted. The films from TMB show excessive pure phase and printing line defects in vertical the printing direction due to slow volatilization speed and low adhesion, while Tol-based films present printing line defects along the printing direction due to large surface adhesion are demonstrated. In contrast, the films from non-halogenated solvent, o-XY exhibited a suitable phase separation size and excellent large-area homogeneity. Consequently, the fully printed 1 cm^2 FOSCs exhibit an efficiency of 14.81%. Moreover, the FOSCs module with an area of 28–104 cm^2 gives an efficiency of over 13%, with a CTM of 0.9. Selecting suitable non-halogenated solvents to achieve large-area uniformity and appropriate phase separation morphology in >100 cm^2 modules is of great importance for the industrialization of FOSCs.

1. Introduction

Organic solar cells (OSCs) have the advantages of flexibility, lightweight, low cost, and green solvent processing.[1–4] Among them, large-area flexible organic solar cells (FOSCs) are extensively studied due to their significant commercialization potential in building-integrated photovoltaics and flexible wearable electronics.[5–7] Recently, with the development of donor and acceptor materials, as well as fabrication techniques, the efficiency of FOSCs developed quickly in the past years. Hou, Wei, Chen, and Zhou et al. reported efficiencies of 13.5% (23.6 cm^2),[8] 13.25% (46 cm^2),[9] 15.4% (25 cm^2),[10] 14% (41 cm^2)[11] for the FOSCs module. For the practical application, it is needed to further develop the fast R2R fabrication technology for producing large-area modules with an area >100 cm^2. Nowadays, the cell-to-module efficiency remaining (CTM) ratio is still lower, particularly for modules with an area larger than 100 cm^2, which means high-efficiency loss during upscaling.[12,13] Until now, most of the work reported a CTM of 0.7–0.8 for modules with an area of 10–20 cm^2, and a few works showed a higher CTM of around or higher than 0.9.[14] For devices with an area larger than 100 cm^2, flexible modules with high efficiency and high CTM were rarely reported. Therefore, upgrading the CTM for printed devices is significantly important for the further development of FOSCs.

S. Yang, F. Guo
Henan Institutes of Advanced Technology
Zhengzhou University
Zhengzhou 450052, P. R. China
E-mail: fqguo@zzu.edu.cn

S. Yang, X. Chen, Y. Pan, J. Fang, Y. Han, Z. Wang, F. Qian, W. Qi, K. Shui, C.-Q. Ma, Q. Luo
i-Lab & Printable Electronics Research Center
Suzhou Institute of Nano-Tech and Nano-Bionics
Chinese Academy of Sciences (CAS)
Suzhou 215123, P. R. China
E-mail: cqma2011@sinano.ac.cn; qluo2011@sinano.ac.cn

The ORCID identification number(s) for the author(s) of this article can be found under https://doi.org/10.1002/adma.202500115

DOI: 10.1002/adma.202500115

C.-Q. Ma, Q. Luo
School of Nano-Tech and Nano-Bionics
University of Science and Technology of China
Hefei 230027, P. R. China

Q. Zhang
Vacuum Interconnected Nanotech Workstation (Nano-X)
Suzhou Institute of Nano-Tech and Nano-Bionics
Chinese Academy of Sciences (CAS)
Suzhou 215123, P. R. China

Y. Sun
School of Chemistry
Beihang University
Beijing 100191, P. R. China
E-mail: sunym@buaa.edu.cn

For the bulk heterojunction OSCs, the solvents for processing the active layer play a decisive role in the microscopic morphology, that is, the phase separation size, aggregation, and crystallization and determine the device performance.[15–18] Nowadays, low-boiling-point halogenated solvents, such as chloroform (CF) are mostly used for the fabrication of high-efficiency non-fullerene OSCs due to their excellent solubility.[19–21] But for the upscaling of OSCs, it is necessary to utilize higher-boiling-point green solvents to enable the fabrication of large-area films without environmental pollution.[22–25] In recent years, a series of works demonstrated highly efficient OSCs using non-halogenated solvents. For example, Ma et al. fabricated a series of devices based on PM6:BTP-eC9 and PM6:L8-BO using chloroform (CF), chlorobenzene (CB), and o-xylene (o-XY). BTP-eC9 was noted for its good solubility and was found to exhibit appropriate phase separation morphology during the slow film formation process caused by high-boiling-point solvents, resulting in a power conversion efficiency (PCE) of 18.25% by blade coating.[26] Yang et al. proposed a hot solution strategy to improve the performance of OSCs based on two high-boiling-point solvents: halogenated solvent chlorobenzene (CB) and non-halogenated green solvent o-xylene (o-XY). In situ measurements and morphological characterization revealed that hot solution facilitates rapid and synchronous molecular assembly of donor and acceptor, which enables the formation of optimized vertical phase separation and molecular packing, thereby enhancing charge generation and extraction.[27]

For the R2R printing of OSCs, the use of different solvents would lead to different phase separation micromorphology due to variations in evaporation rate during printing. Besides the phase separation morphology, solvents also influenced a lot for the large-area homogenous. The main reason for the low CTM of the printed FOSCs is due to the inhomogeneity of the large-area films. It is well known that spin-coated films generally exhibit good film uniformity because of centrifugal force and suitable microstructure due to quick drying dynamics.[28,29] However, for R2R printing, the natural leveling and droplet merging process of printing may cause film defects and uniformity of the film.[30] Only ink with proper rheology properties, that is, viscosity, surface energy, and evaporation rate could enable the formation of large-area homogenous film. For instance, if the viscosity is too fast, the ink droplets can't merge well, resulting in periodic string-like structures and causing unevenness in the film.[31,32] If the evaporation rate is slow, the ink droplets excessively flow on the substrate, leading to unevenness. Therefore, the solvent significantly influences both the macroscopic and microscopic morphology of the active layer for the printed OSCs and consequently impacts the device performance during upscaling. However, the detailed evaluation criteria of the solvents for the R2R printing of organic active layer has not been reported yet as far as we know.

In this work, we achieved a high cell-to-module efficiency remaining ratio for the R2R printed FOSCs at a speed of 50 m min^{-1} by systematically manipulating the macro morphology and micromorphology of the printed active layer through solvent engineering. Three high-boiling-point non-halogen solvents were used as models in this study. Among Tol, o-XY, and TMB, o-XY was identified as the most suitable solvent for large-area printing, which showed the balance of phase separation morphology and large-area film uniformity due to proper viscosity, adhesion force, and evaporation speed. Based on this, a 1 cm^2 monolithic device with a PCE of 14.81% was achieved. The flexible modules with an active area of 28–104 cm^2 showed high PCEs of over 13%, which represents the efficiency record of the FOSCs processed from fully R2R printing. In addition, the CTM was ≈0.9, showing great potential for the up-scale of this method. This work shows the great potential of o-XY-based R2R gravure printing for mass fabrication of FOSCs.

2. Results and Discussion

2.1. Large-Area Flexible Organic Solar Module

In this work, flexible large-area modules with an active area of 28, 52, 80, and 104 cm^2 were fabricated using fully gravure printing technology with o-XY solvent. In these modules, the flexible Ag-NWs electrode, the ZnO electron transporting layer (ETL), and the active layer were subsequently fabricated through R2R printing. **Figure 1a** shows the schematic diagrams of gravure printing, and Figure 1b shows the molecular structure of the donor PM6 and the acceptor BTP-BO-4Cl and the solvents. The modules of 28, 52, and 80 cm^2 consist of 7, 13, and 20 sub-cells that connected through a series connection, each one with an area of 4 cm^2. The 104 cm^2 large-area module was connected through series and parallel connecting of 26 sub-cells.

The schematic diagrams and the photographs of the flexible module are shown in Figure 1c and the J–V characteristics of these modules are shown in Figure 1d and **Table 1**. For the large-area module with active areas of 28, 52, 80, and 104 cm^2, a similar high efficiency of over 13% was achieved. Take the 80 cm^2 module as an example, the open-circuit voltage (V_{OC}), short-circuit current (J_{SC}), fill factor (FF), and PCE were 15.443 V, 1.21 mA cm^{-2}, 70.24%, and 13.13%, respectively. With the increase of device area from 28 to 104 cm^2, the module efficiency of the fully R2R printed OSCs maintains a consistent level. This observation robustly confirms the superior uniformity of the large-area thin films, which suggests the promising potential for mass production. In addition, the 1 cm^2 FOSCs were also fabricated in this work, and the PCE of 1cm^2 PM6:BTP-BO-4Cl flexible device gave an efficiency of 14.81%, which is among the highest reported data for the R2R gravure printed, R2R blade coated and R2R slot-die coated flexible OSCs in recent years (Figure 1e, Table S1, Supporting Information).

For the development from laboratory to commercialization, the cell-to-module (CTM) efficiency remaining ratio from monolithic devices to large-area module devices indicates the potential for process scaling, making it an important metric, thereby we summarized the results in the recent works.[33] We can find that most of the CTM is among 0.7–0.8 for modules with an area larger than 10 cm^2, while rare work reported a CTM value nearly or higher than 0.9. Feng et al.[14] achieved a CTM value of 0.92 for the 11.08 cm^2 module, Zhu et al.[34] achieved a CTM value of 0.82 for the 17.6 cm^2 module, Lu et al.[11] achieved a CTM value of 0.87 for the 41 cm^2 module. However, these works are all related to the module with an area smaller than 50 cm^2. For the flexible module with an area larger than 100 cm^2, only Kown et al.[35] demonstrated a module with a CTM value of 0.81 and a PCE of 9.15% for the FOSC with an area of 108 cm^2 (Figure 1f, Table S2, Supporting Information). Here, we reported a high CTM of

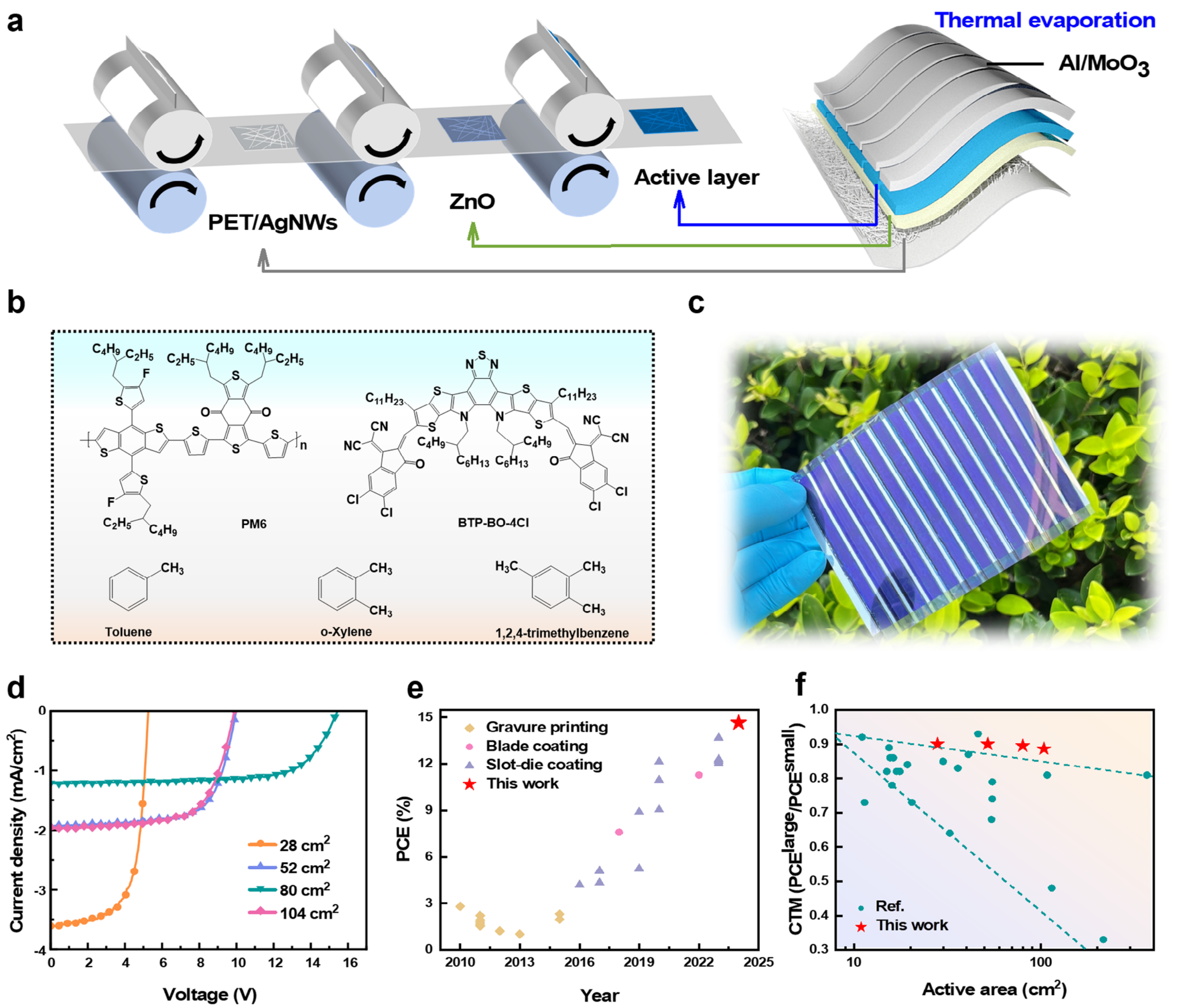

Figure 1. a) Schematic diagram of a flexible module made from gravure-printed layers. b) The molecular structure of the donor PM6 and the acceptor BTP-BO-4Cl and three solvents. c) Photograph of the module. d) *J*–*V* characteristics of modules with 7, 13, and 20 sub-cells connected in series. e) Summary of the efficiency of flexible OSCs fabricated by gravure printing and other roll-to-roll techniques in recent years.[29,36–51] f) Plot of CTM ratio for large-area modules versus active area (>10 cm^2) in recent years.[7,9,11,14,33–35,52–65]

≈0.9 for the R2R-printed flexible OSC with a higher efficiency of over 13%. Additionally, it is worth noting that the bottom AgNWs electrodes, the ZnO ETL layer, and the active layers were all fabricated through continuous R2R gravure printing at a speed of 50 m min^{-1}. Such a result confirms the future potential of R2R gravure printing for the preparation of large-area FOSCs.

Table 1. Device performance of the fully R2R gravure printed FOSCs modules.

Area [cm^2][a)]	V_{OC} [V]	J_{SC} [mA cm^{-2}]	FF [%]	PCE [%]
28	5.328	3.60	69.10	13.25
52	9.986	1.93	68.80	13.26
80	15.443	1.21	70.24	13.13
104	9.891	1.95	67.41	13.00

[a)] The area is the effective area.

2.2. Solvent-Dependent Large-Area Homogeneity

For the fabrication of large-area FOSCs, the macroscopic morphology of the film, such as uniformity and pinholes, significantly affects the photovoltaic performance of the devices. In this work, we compared the influence of three different solvents, that is, Tol, o-XY, and TMB. First of all, the boiling points of Tol, o-XY, and TMB were 110.6 °C, 144.4 °C, and 168.9 °C, respectively (**Figure** 2a). The solubility parameters for the acceptor and the solvent were calculated using the group contribution method,[27]

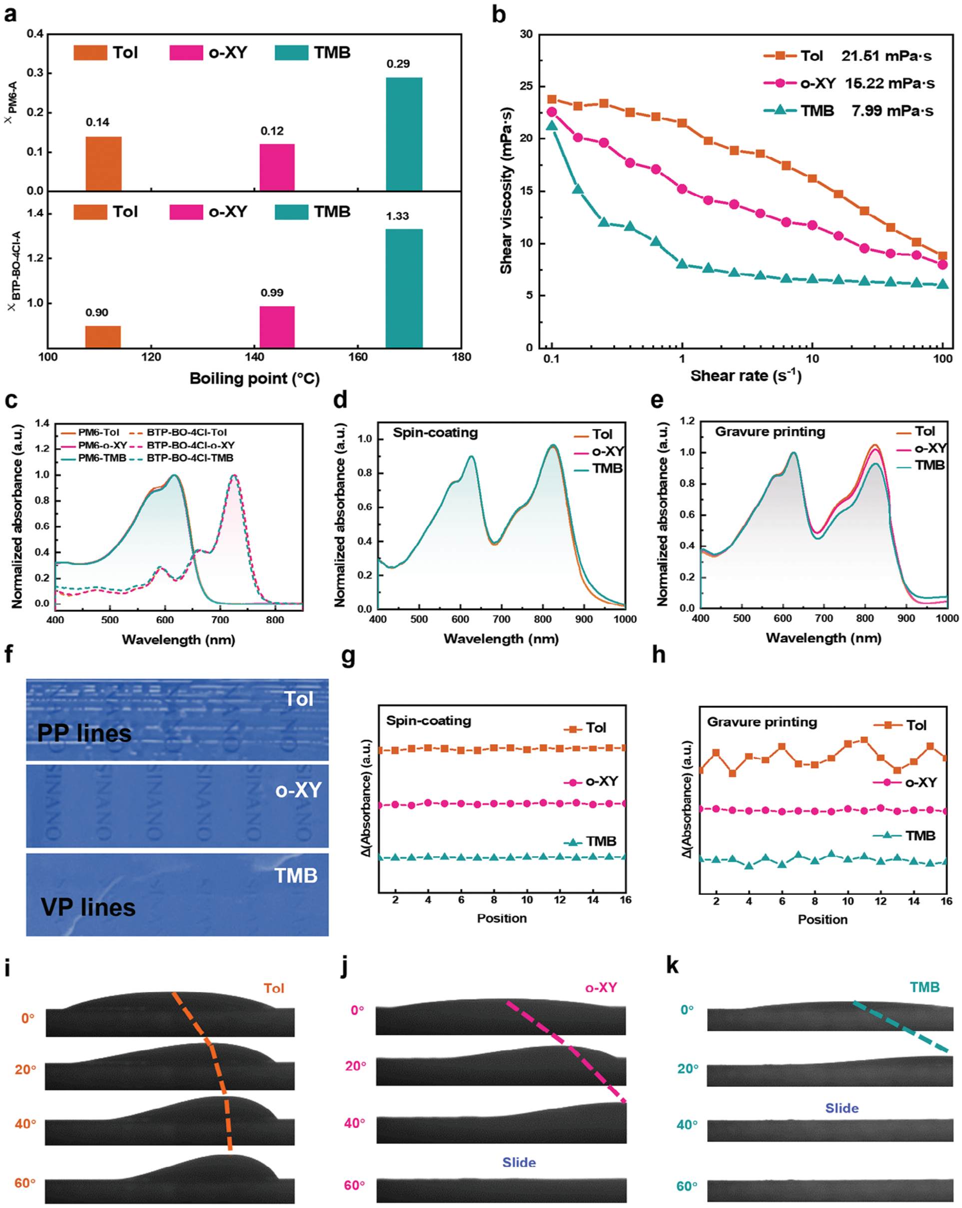

Figure 2. a) Solvent classification diagram based on boiling points and donor–acceptor material interaction parameters. b) Relationship between shear viscosity and shear rate for active layer inks with Tol, o-XY, and TMB. c) Normalized absorption spectra of PM6 and BTP-BO-4Cl in different solvents. Normalized absorption spectra of d) spin-coated e) gravure printed active layer films prepared from different solvents. f) Photographs of the gravure printed films processed from Tol, o-XY, and TMB. Absorption uniformity of g) the spin-coated films and h) the gravure printed films processed from Tol, o-XY, and TMB. Contact angle images of active layer ink with i) Tol, j) o-XY, and k) TMB on ZnO substrate in a horizontal state and at an angle of 0°, 20°, 40°, and 60°.

and based on these results, the interaction parameters between them were calculated and listed in Table S3 (Supporting Information). The interaction parameters between PM6 and the three solvents were 0.14, 0.12, and 0.29, respectively, indicating that PM6 has similar solubility in Tol and o-XY, but with better solubility compared to TMB. For the BTP-BO-4Cl, the interaction parameters with Tol, o-XY, and TMB were 0.90, 0.99, and 1.33, respectively, which means BTP-BO-4Cl has the highest solubility in Tol, followed by o-XY, and TMB. The rheological properties of the printed inks processed from different solvents, including viscosity, and surface tension are shown in Figure 2b. The viscosities were estimated to be 21.51, 15.22, and 7.99 mPa s for the Tol, o-XY, and TMB-based inks.[66] These results indicated the Tol-based inks have a higher viscosity, and a larger surface tension relative to o-XY and TMB. TMB-based inks have a lower viscosity and smaller surface tension relative to Tol and o-XY. The differences in solubility, along with the different rheology properties, that is, drying rates, and viscosity will significantly influence the microstructural and macrostructure morphology. According to the solvent handbook, the viscosity of the three solvents is nearly the same. So, the difference in viscosity of the different solvent inks mainly comes from the interactions between the active layer material and the solvent. For the impact of solvent on viscosity, a good solvent could effectively dissolve materials, leading to a more uniform and lower viscosity. Otherwise, a poor solvent may cause component aggregation and potentially increase viscosity. Additionally, as solvents evaporate, the viscosity tends to rise as well.[67,68] From the interaction parameters in Table S3 (Supporting Information), we can see that the interaction parameters between Tol, o-XY, and the donor are similar, but Tol has stronger interactions with the acceptor material, whereas TMB has weak interaction with donor and acceptor, which results in the difference in the viscosity.

The UV–vis absorption spectra of PM6 and BTP-BO-4Cl in different solvents were measured, and the normalized absorption spectra are shown in Figure 2c. The typical absorption peaks of BTP-BO-4Cl in different solvents showed no significant differences. The maximum absorption peak wavelength of PM6 and BTP-BO-4Cl was determined to be 615 and 725 nm, respectively. However, for PM6 in Tol, the absorption peak ≈582 nm was prominent, indicating a stronger H-aggregation of PM6 in Tol.[69] Subsequently, the UV–vis absorption spectra of the spin-coated and gravure-printed films are shown in Figure 2d,e. The spin-coated blend films from different solvents exhibited nearly identical absorption peaks. However, for the gravure-printed blend films, the absorption peak of BTP-BO-4Cl gradually decreased when transitioning from Tol to o-XY, and TMB, which might be due to the aggregation of acceptor molecules.[70]

To detect the films homogeneity of the printed films, the UV–vis absorption spectra of the large-area films at different 15 regions were measured (Figures S1–S4, Supporting Information). As shown in Figure 2f,g, the spin-coated films processed from different solvents exhibited good film quality and uniformity. In contrast, the gravure-printed films processed from Tol exhibited numerous drying lines and voids, which could be attributed to the excessive rapid drying speed of Tol and poor droplets merging. The printed films from TMB solvents also showed poor homogeneity, which might be due to the excessive movement of ink because of the slow volatilization speed. However, the gravure-printed films processed from o-XY exhibited superior macroscopic morphology and enhanced uniformity (Figure 2h).

We further studied the underlying reasons for solvent-dependent large-area morphology by investigating the contact angle and slide angle of these solvents on the top of ZnO ETL (Figure 2i–k). We know the contact angle stands for the wettability of the droplet on the top of the substrate. However, the substrate is not entirely flat during R2R printing, which makes the inks susceptible to movement due to the influence of gravity. Thus, to thoroughly assess the movement characteristics of the ink during R2R, the slide angle should be investigated as well. The critical slide angle means the minimal angle the inks move on the substrate, which reflects the adhesion force between the inks and the substrates. The quantitative relation between the slide angle and adhesion force could be estimated as:[71,72]

$$F_{\mathrm{adh}} = \frac{k L_{\mathrm{b}} m g \sin \alpha}{w} \tag{1}$$

where L_{b} is the droplet base length, which is the contact surface diameter of a liquid droplet on a solid surface, m is the droplet mass, g is the gravity acceleration, and w is the width of the droplet. Therefore, the larger the sliding angle of the ink droplet on the substrate, the higher the surface tension between the ink droplet and the substrate. For the active layer ink with Tol, the contact angle is ≈19°. In addition, the droplets did not slide at an inclination angle of 0–60°, indicating a large critical slide angle. Such a large contact angle and large slide angle are not favorable for ink leveling, which is the main reason for forming printing lines along the printing direction (PP lines). For the droplet with TMB, the contact angle is only ≈6°, meaning excellent wettability of this droplet. However, the critical slide angle of the droplet on the ZnO substrate is as small as 20°, demonstrating low adhesion force between inks and the substrates. Too low interface adhesion force will lead to uncontrollable movement of inks on the substrate during fast R2R printing, thereby forming printing lines that vertical the printing direction (VP lines). For the o-XY-based droplets, it showed a contact angle of 10°, and a critical slide angle of 40°–60°. The differences in the sliding angles of ink droplets for different solvents primarily arise from the variations in the ink viscosity. As the viscosity of the ink increases, the internal resistance to flow also increases, resulting in stronger cohesive forces within the ink. The enhanced cohesion allows the ink to maintain better contact with the substrate, leading to improved adhesion, while lower-viscosity inks are more prone to spreading or bleeding.[71,72] This observation suggested a proper wettability and adhesion force of the o-XY-based inks with the substrate, thereby leading to good ink leveling and homogenous films with fewer defects. According to this result, we can confirm that the solvent with an intermediate surface adhesion and surface energy is essential for ensuring large-area homogeneity.

2.3. Solvent-Dependent Phase Separation Morphology of Printed Organic Films

Besides large-area homogenous, the phase separation morphology plays a more important role in the device performance. It is well known that for the bulk heterojunction OSCs, the microscopic morphology of the active layer is not only composed of the donor and acceptor phases but also the donor–acceptor mixed amorphous blended phase. Variations in the mixed-phase components influenced the exciton dissociation and diffusion efficiency and finally affected the photovoltaic performance of OSCs.[73,74] According to the work of *Ade* et al., the relationship between component content and intermolecular interactions in the blended phase can be divided into three cases based on the Flory–Huggins χ. One case represents a low χ between the donor and acceptor, which means good miscibility and will form a more mixed phase. The second case represents a moderate χ between the donor and acceptor so that the acceptor content in the blended phase is sufficient for the percolation threshold, facilitating exciton dissociation and carrier transport. The third case indicates a high χ value between donor and acceptor, where the phase separation is too pure.[75]

To study the changes in the blended films processed from different solvents, the absorption shift as a function of molecular concentration was investigated. As we know, a redshift of the absorption peaks is often observed when the NFA molecules are in aggregated states (e.g., in the neat film), compared with monomer states (such as in dilute solution).[76–78] The PM6:BTP-BO-4Cl films with different weight ratios of donor and acceptor were studied (Figure S5; Table S4, Supporting Information). **Figure** 3a–i shows the UV–vis absorption spectra of the blend films with varying BTP-BO-4Cl content processed from different solvents, as well as the change of the absorption peak ($\lambda_{\mathrm{abs}}^{\mathrm{max}}$) of acceptor in these films. Take the blend films processed from o-XY as an example. For the spin-coated films with BTP-BO-4Cl concentration of 0.01, the maximum absorption peak of BTP-BO-4Cl is 783 nm, showing red-shift compared to that in the solution ($\lambda_{\mathrm{abs}}^{\mathrm{max}}$ = 725 nm). Such a red-shifted absorption wavelength indicated the change in molecular environments. As the concentration of BTP-BO-4Cl increases to 0.04, the change in $\lambda_{\mathrm{abs}}^{\mathrm{max}}$ is minimal. Further increasing the BTP-BO-4Cl blend ratio leads to a gradual redshift of $\lambda_{\mathrm{abs}}^{\mathrm{max}}$ of BTP-BO-4Cl until the formation of a continuous acceptor crystalline phase at a maximum saturates of 824 nm. According to the saturation of $\lambda_{\mathrm{abs}}^{\mathrm{max}}$ to Figure 3c, the critical blend ratio for the formation of the acceptor phase (C_{AP}) is determined to be 0.60, which means that BTP-BO-4Cl turns to crystalline domains when the blend ratio is higher than 0.60. In other words, the maximum blend ratio of BTP-BO-4Cl in the intermixed phase is 0.60. If further increasing the content of the acceptor, BTP-BO-4Cl will self-aggregate to form the pure acceptor phase. Similarly, for gravure printed films processed from o-XY, the critical blend ratio for the formation of C_{AP} is also determined to be 0.60. Hence, it is evident that the maximum non-fullerene acceptor (NFA) ratio in the mixed phase of active layers is nearly the same, whether processed by spin-coating or gravure printing with o-XY. However, the C_{AP} values in the spin-coated and gravure-printed films processed from Tol are determined to be 0.65 and 0.90, respectively. The much higher BTP-BO-4Cl concentration in the intermix phase for the Tol-based printed films indicated that PM6 and BTP-BO-4Cl were more miscible compared to the active layer processed by spin coating. As a result, fewer acceptor pure phases were formed in the printed films, which could potentially hinder charge transport and extraction. On the other hand, the C_{AP} value in the spin-coated and gravure-printed blend films processed from TMB is determined to be 0.60 and 0.50, respectively. It means that the concentration of BTP-BO-4Cl in the gravure printed film was lower than that in the spin-coated films. The higher content of the pure phase might lead to higher non-radiative recombination, which could be the reason for V_{OC} and FF losses in the gravure printed devices processed from TMB.[79]

The AFM images of the films from different solvents were measured to further investigate the microscopic morphology of the active layer films (Figure 2j–l; Figure S6, Supporting Information). The gravure-printed films showed coarser fibers and greater aggregation than the spin-coated films. The gravure-printed films processed from Tol exhibited finer fiber structures and smoother surfaces, while the gravure-printed films processed from TMB displayed coarser fiber structures and increased roughness.[80]

The 2D grazing-incidence wide-angle X-ray scattering (2D GIWAXS) measurement was conducted to assess the molecular orientation and crystallization for gravure printed films processed from three solvents. 2D GIWAXS patterns and integrated scattering profiles of the films processed from three solvents along the IP and OOP directions were shown in Figures S7,S8 (Supporting Information). All three solvent-processed films showed similar strong edges on orientation at 0.31 Å^{-1} and face on orientation at 1.74 Å^{-1}. By fitting the 2D curves, we obtained the π–π stacking distances of 3.59, 3.58, and 3.58 Å for the films in the out-of-face direction, respectively, all of which exhibit similar tight stacking. The calculated crystal coherence length of the (010) peak were 25.80, 25.75, and 25.11 Å, respectively. These results indicated that the crystallinity of the gravure-printed films processed with different solvents was similar. The 2D GISAXS data for the gravure printed films processed from different solvents are shown in Figure 2m–o. The radius of gyration (R_{g}) of the BTP-BO-4Cl domain was calculated using the Guinier approximation method according to the following equation:[81]

$$I(q) = I(0)\exp\left(-\frac{q^2 R_g^2}{3}\right) \tag{2}$$

$I(q)$ is the scattering intensity at q and $I(0)$ is the zero-angle scattering intensity. The average grain size could be calculated using the R_{g} extracted from the slope of $\ln(I(q))$ in the low-q region (0.005–0.02 Å). As a result, the domain sizes of BTP-BO-4Cl in the gravure-printed films processed from Tol, o-XY, and TMB were ≈84.5, 91.9, and 111.2 nm, respectively. The increase in domain sizes is in good agreement with the results obtained from the previous UV–vis absorption spectra.

2.4. Underlying Mechanism and Solvent Selective Guidelines for Large-Area R2R Printing

To clearly show this dynamic process of ink drying and phase separation, in situ time-resolved absorption spectra of the films during spin-coating (**Figure** 4a–f) and gravure printing were measured (Figures S9,S10, Supporting Information). As shown in Figure 4a–f, the film formation process can be divided into three stages: solvent evaporation (step I), nucleation and crystal growth (step II), and dried film (step III).[82] In the first stage, the solvent evaporates gradually, and the absorption peak position remains unchanged. As the solution reached its solubility limitation, this process transferred from step I to step II. In this stage, the organic molecule begins to aggregate and crystallize. Correspondingly, the absorption peak redshifts gradually. Typically, the aggregation rate is represented by calculating the slope of the second-stage curve.[82–84] Finally, the absorption peaks remain constant since no change in the molecular aggregate morphology occurred, which could be named step III. As shown in Figure 4a–f, both the solvent drying duration (step I) and the nucleation and crystal growth duration (step II) for the Tol, o-XY, and TMB solvents systems are different either in the spin-coating process or in the gravure printing. In step I, since the organic molecules are kept in a single molecular state, the molecular aggregation states would not be influenced by the change in drying speed. However, the solvent drying time significantly influenced the ink movement. Thus, it is important to analyze the solvent evaporation time and understand the underlying mechanism of the ink rheology process. In this work, the solvent evaporation time of step I (Figure 4g) during the spin-coating process from

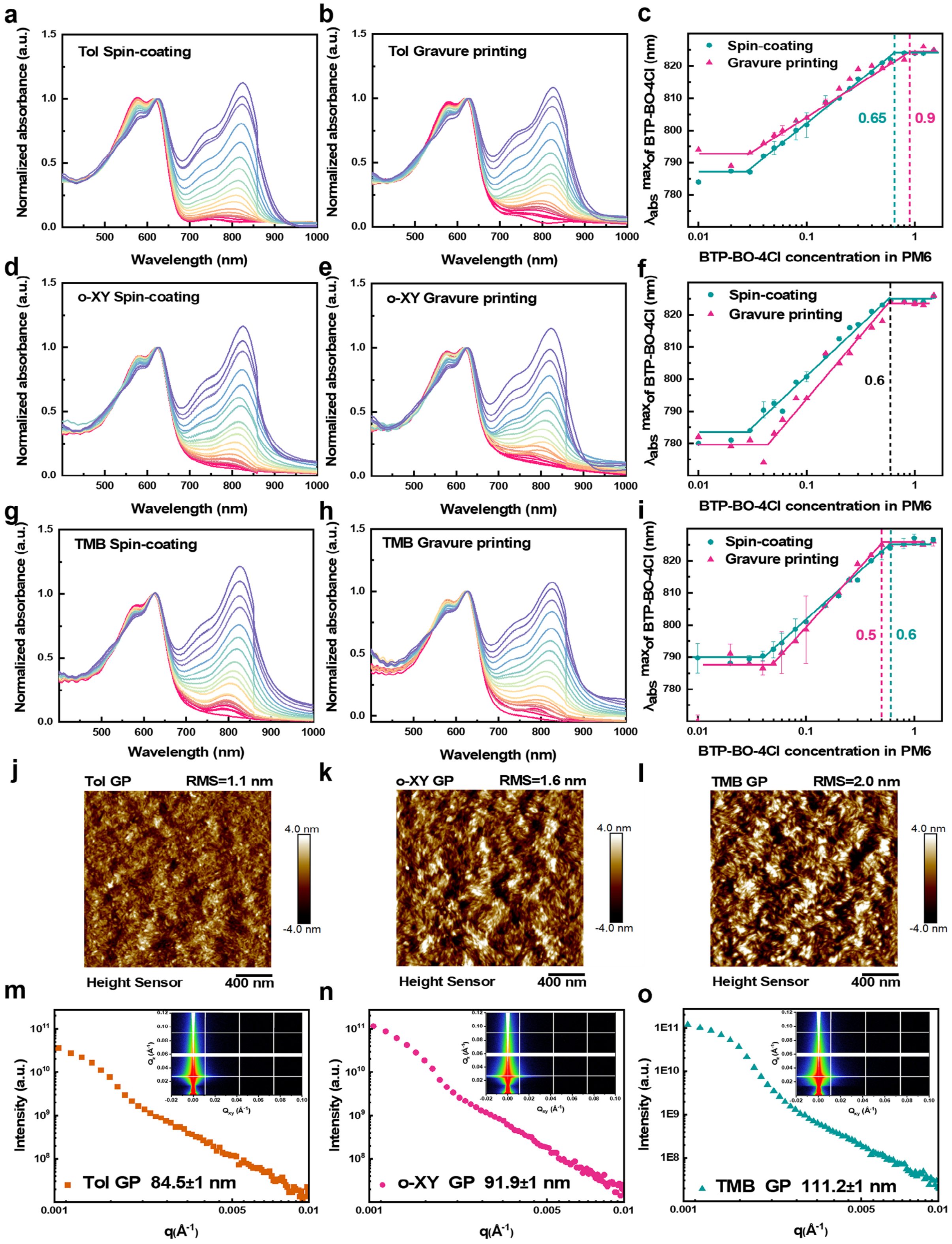

Figure 3. The normalized UV–vis absorption spectra of the spin-coated films processed from a) Tol, d) o-XY, g) TMB solvent, and the gravure printed films processed from b) Tol, e) o-XY, and h) TMB solvent. Evolution of the BTP-BO-4Cl absorption peak in the films from c) Tol, f) o-XY, and i) TMB solvents and the error bars represent the standard deviation for three independent samples. AFM images of the gravure printed blend films processed from j) Tol, k) o-XY, and l) TMB. The 2D GISAXS images and the 1D profiles of the gravure printed blend films processed from m) Tol, n) o-XY, and o) TMB.

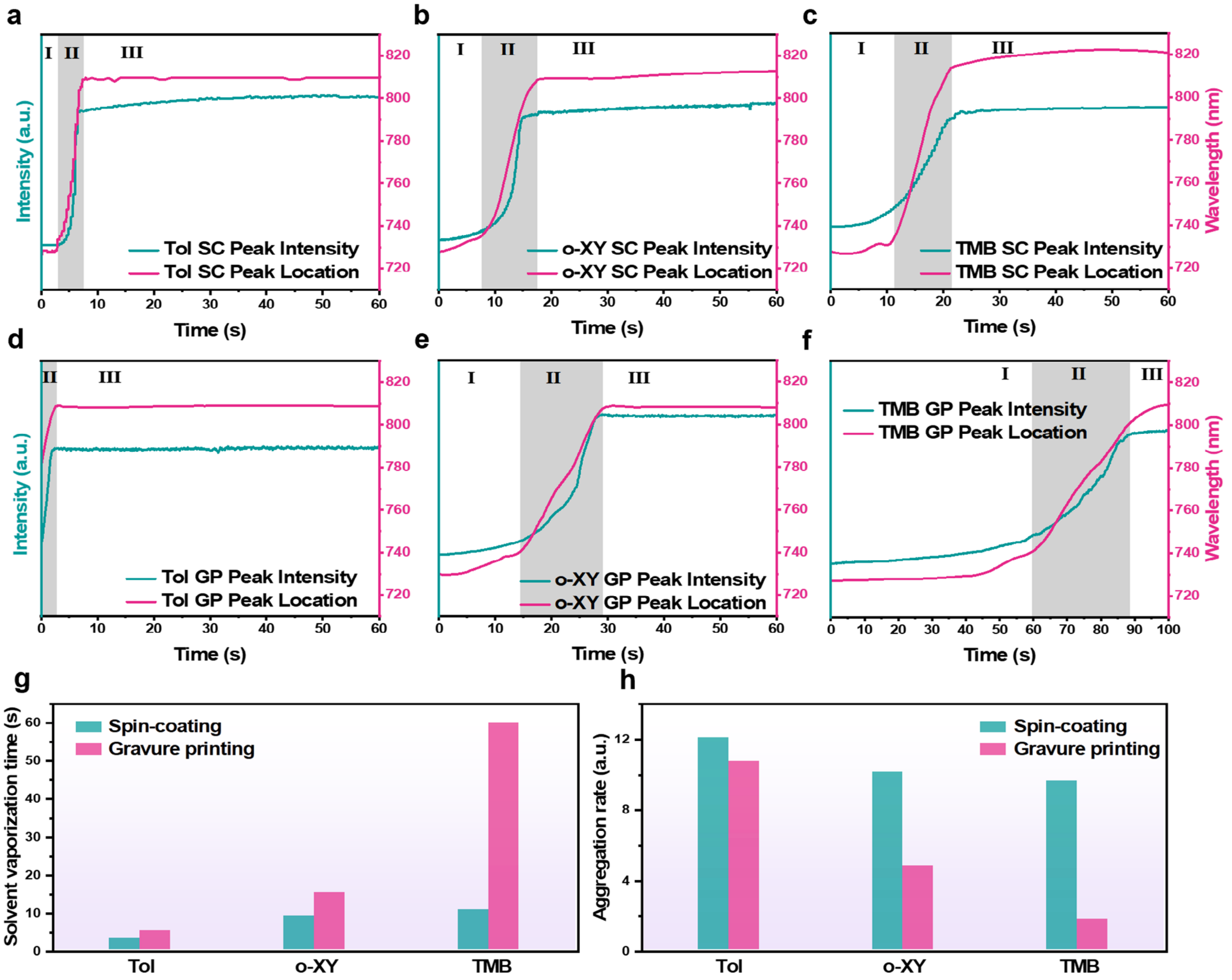

Figure 4. The time-dependent intensity and location evolution of BTP-BO-4Cl 0-0 peak for spin-coated blend films processed from a) Tol, b) o-XY, c) TMB, and for gravure printed blend films processed from d) Tol, e) o-XY, f) TMB. g) Solvent vaporization time of BTP-BO-4Cl in blend films, and h) aggregation rate of BTP-BO-4Cl in blend films.

different solvents are similar, which were 3.0, 8.9, and 10.5 s for the Tol, o-XY, and TMB systems, respectively. In contrast, the solvent evaporation time during gravure printing from Tol, o-XY, and TMB were 5, 15, and 60 s, respectively. Such a big difference in solvent evaporation time among the gravure-printed films processed from different solvents was another reason for different film uniformity.

The slope of the acceptor absorption peak position versus time during the second step (step II) was calculated to quantify the aggregation rate. In the spin-coating process, the aggregation rates of the films using Tol, o-XY, and TMB solvents were 12.08, 10.13, and 9.62, respectively, exhibiting minor differences among different solvents. However, in the gravure printing process, the aggregation rates for films produced using Tol, o-XY, and TMB were significantly different, with values of 10.72, 4.77, and 1.75, respectively (Figure 4h). These results indicated that the Tol processed gravure printing process exhibited an extremely rapid aggregate and nucleation without sufficient time for crystallization of BTP-BO-4Cl, thereby leading to a higher concentration of BTP-BO-4Cl in the intermix phase. In the case of TMB, prolonged nucleation and crystallization time led to large-scale liquid–liquid phase separation, resulting in extended nucleation and crystallization for the small molecules. Consequently, the active layer exhibited a larger phase separation size, with a much lower concentration of BTP-BO-4Cl in the intermix phase and a higher content of pure phases. This observation is consistent with the result of the low absorption intensity of BTP-BO-4Cl for the gravure-printed films processed with TMB (Figure S5, Supporting Information).

Based on the aforementioned results, it is evident that the solvent highly influenced the microstructure and macrostructure of the films. In terms of microstructure morphology, the films processed from o-XY exhibited a suitable phase separation size, which ensured a balanced exciton dissociation and charge transport process. The films processed from Tol, on the other hand, exhibited excessive mixed phases, while the TMB-based films showed an excessive amount of pure phase, both of which

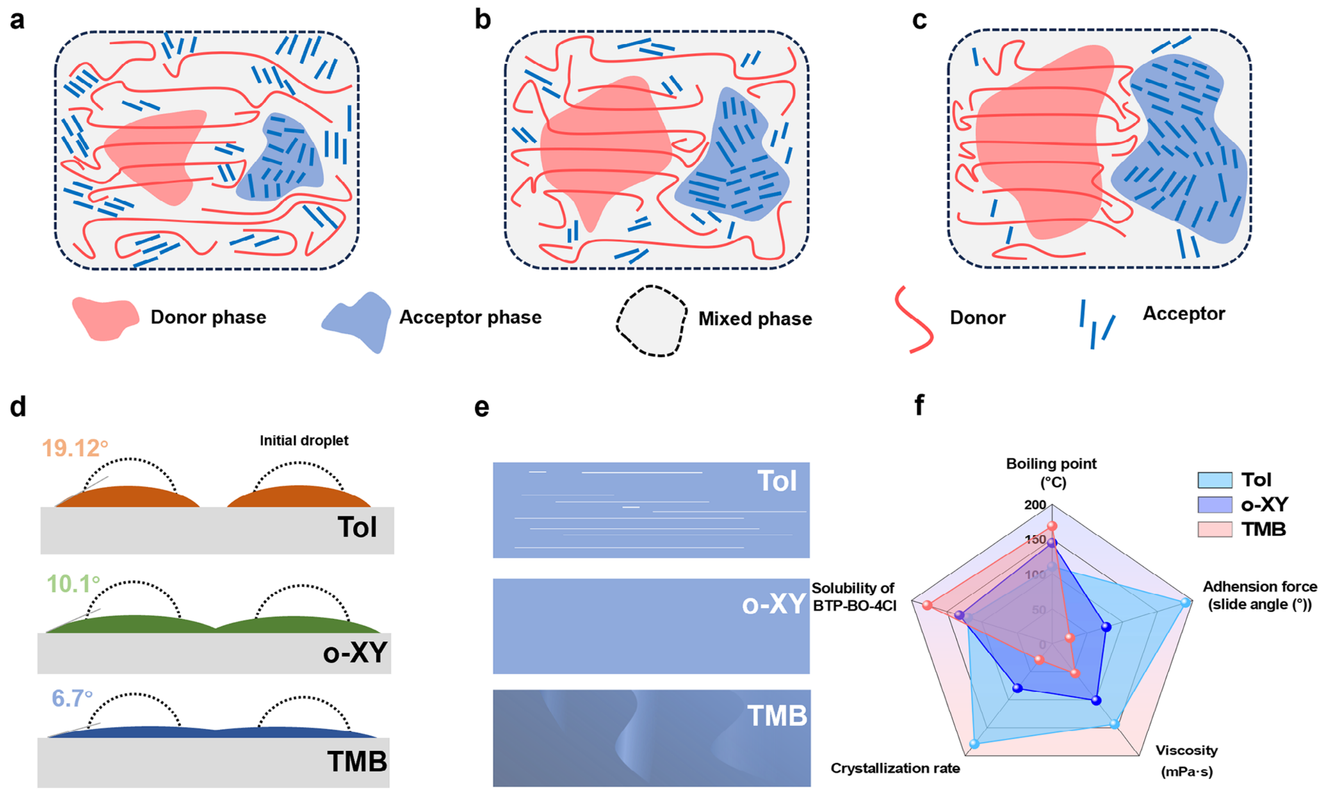

Figure 5. Schematic diagram of the donor–acceptor distribution in the active layer of the gravure printed blend films processed from a) Tol, b) o-XY, c) TMB. d) Schematic of the fusion of ink droplets of three solvents on a substrate. e) Schematic diagram of the macroscopic morphology of gravure printed film processed from Tol, o-XY, TMB. f) Pentagonal matrix analysis of boiling point, adhesion, viscosity, crystallization rate, and solubility parameters of three solvents.

would cause poor device performance (**Figure** 5a–c).[75] Regarding macrostructure morphology, the influence mechanism of solvent could be described by Figure 5d,e. A large contact angle and slide angle for the Tol solvent caused difficulty in droplets merging effectively. In contrast, a small contact angle of TMB can allow well droplet merging. However, the excessively low slide angle will lead to uncontrollable movement of inks. Thus, two typical defects in the large-area films, PP lines, and VP lines would be formed when the inks have too high or low adhesion force with the substrates. A moderate adhesion force, as well as suitable dying speed, and surface energy, are important for achieving large-area homogeneity.[85,86] Based on the above results, we know the solvents for R2R printing should be evaluated from the following five aspects: boiling point, adhesion, viscosity, crystallization rate, and solubility (Figure 5f).

2.5. Device Performance of Printed Organic Solar Cells

Flexible OSCs with an inverted structure of PET/AgNWs/ZnO/PM6: BTP-BO-4Cl/MoO_3/Al were fabricated. In this structure with AgNWs bottom electrode, it is better to deposit thicker MoO_3 hole transporting layer (HTL) to avoid short-circuit of the device caused by the large roughness. For the device with an Al top electrode, the MoO_3 layer can be increased to 20 nm, which is much thicker than the device with an Ag top electrode. Therefore, the Al top electrode rather than the Ag electrode was deposited on the top MoO_3 HTL in this work.[87] Due to the influence of solvents on the large-area homogeneity and phase separation morphology, the printed FOSCs processed from different solvents showed huge different device performance. The highest efficiency of 14.81% for 1 cm^2 flexible OSCs was achieved when o-XY solvent was used, while devices processed from Tol and TMB gave a relatively lower efficiency of 10.98% and 11.69%. The spin-coated devices processed from different solvents exhibited similar performance, with an average efficiency of ≈14.5% (**Figure** 6a, and **Table** 2).

Compared to the spin-coated devices, the gravure-printed devices exhibited a slightly higher J_{SC}, which is related to the thickness of the active layer. The thickness of the spin-coated films for the optimal conditions was ≈120–140 nm, while that of the gravure-printed films was ≈160–180 nm. We also observed devices processed from Tol and TMB have lower V_{OC} and FF. It has been reported that the excess of pure phase led to an increase in the non-radiative recombination losses, which in turn results in the loss of V_{OC} or FF.[75,79,88,89] In this work, the critical blend ratio for the formation of the acceptor phase (C_{AP}) in printed films from Tol, o-XY, and TMB solvent was 0.90, 0.60, and 0.50. The real D/A ratio is 1:1.2, which means different acceptor pure phase volumes in the real printed films. In the Tol-based printed films, there was a higher BTP-BO-4Cl concentration in the intermixed phase, while in the TMB-based printed

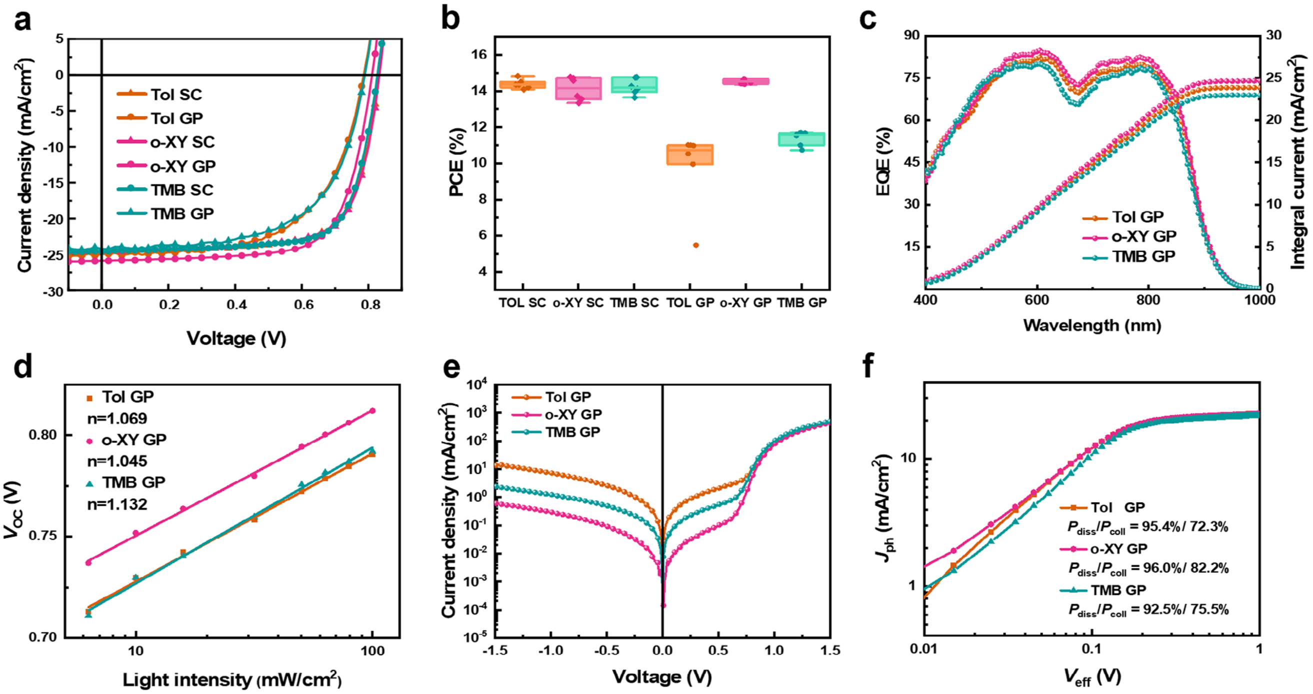

Figure 6. a) J–V curves of flexible devices processed from different solvents. b) Histogram of power conversion efficiency (PCE) of the spin-coated and gravure-printed flexible solar cells calculated by 6 devices with different solvents. c) EQE curves for gravure printed flexible devices processed from different solvents. d) Light-intensity-dependent V_{OC} for gravure printed flexible devices processed from different solvents. e) Dark J–V curves for the gravure printed flexible devices processed from different solvents. f) Photocurrent density (J_{ph}) as a function of effective voltage (V_{eff}) for gravure printed flexible devices processed from different solvents.

films, there was a higher content of the acceptor pure phase. The exitance of the excess pure phase caused large acceptor aggregation and led to non-radiative losses of the devices. Ultimately, the appropriate acceptor content in mixed-phase printed devices processed with o-XY satisfies the percolation threshold requirement and leads to higher FF. The lower V_{OC} of the Tol-based device was caused by film defects. The performance histogram showed the gravure-printed devices (Figure 6b, and Table 2) processed from o-XY exhibited a much higher average performance as well.

The EQE spectra (Figure 6c) of the o-XY-based devices also exhibited a higher photon utilization efficiency, with an external quantum efficiency of ≈80%, which is slight higher than the spin-coated devices (Figure S11a, Supporting Information). However, a significant decrease in the EQE spectrum was noted at 700 nm. Based on the result of the standard rigid devices and the

Table 2. Photovoltaic performance of 1cm^2 flexible devices processed from different solvents under the illumination of an AM 1.5G solar simulator, 100 mW cm^{-2}.

Active layer process method	Solvent	V_{OC} [V]	$J_{SC}/J_{int.}$ [mA cm^{-2}]$^{a)}$	FF [%]	PCE$^{b)}$ [%]
Spin-coating	Tol	0.830	24.80/23.64	72.02	14.82
		0.831 ± 0.003	24.70 ± 0.17	69.76 ± 2.96	14.42 ± 0.65
	o-XY	0.831	24.50/23.33	72.27	14.71
		0.830 ± 0.002	24.65 ± 0.21	69.76 ± 2.59	14.28 ± 0.59
	TMB	0.826	24.50/23.34	72.89	14.75
		0.826 ± 0.001	24.67 ± 0.22	71.11 ± 0.50	14.25 ± 0.41
Gravure printing	Tol	0.780	25.04/23.85	56.29	10.99
		0.779 ± 0.001	24.60 ± 0.53	56.11 ± 0.18	10.79 ± 0.28
	o-XY	0.810	25.86/24.63	70.71	14.81
		0.809 ± 0.001	25.32 ± 0.24	71.30 ± 0.37	14.61 ± 0.10
	TMB	0.788	24.10/22.95	61.57	11.69
		0.788 ± 0.002	24.13 ± 0.22	61.67 ± 0.71	11.37 ± 0.37

a) Integrated current density based on EQE curves; b) Averages and standard errors of PCEs.

absorption spectra of the films, the low absorption intensity of the blended film at 700 nm is responsible for this result (Figure S11b, Supporting Information).

The dependence of J_{SC} and V_{OC} on light power (P_{light}) was measured to study the charge recombination (Figure 6; Figures S12,S13, Supporting Information). First, the relationship between V_{OC} and P_{light} was analyzed using the following equation: $V_{OC} \propto nkT/q\ln P$ (k is the Boltzmann constant, q is the elementary charge, and T is the temperature). Extracted from Figure 6d, the fitted n values for the gravure-printed flexible devices processed from Tol, o-XY, and TMB were 1.069, 1.045, and 1.132 kT/q, respectively, indicating the lowest trap-assisted and monomolecular recombination in the o-XY-based device. Additionally, the relationship between J_{SC} and P_{light} was investigated according to the equation of $J_{SC} \propto P_{light}{}^{\alpha}$, where the parameter α represents the exponent factor. When the value of α approaches 1,[90] it indicates more effective suppression of bimolecular recombination under short-circuit conditions. Figure S13 (Supporting Information) showed that the α values for the gravure-printed flexible devices processed from Tol, o-XY, and TMB were 0.933, 0.934, and 0.935, respectively. The light-intensity-dependent V_{OC} and J_{SC} of the spin-coated devices from different solvents are similar (Figure S12, Supporting Information), suggesting slight differences in bimolecular recombination among the devices processed from different solvents. Further, the rectification ratios of the gravure-printed flexible devices processed from Tol, o-XY, and TMB (Figure 6e) were determined to be 35, 720, and 210. The gravure-printed flexible devices processed from o-XY exhibited a higher rectification ratio, indicating more effective charge selectivity, which is expected to contribute to the improvement of FF.

Further, we studied the exciton dissociation and charge collection mechanism in the printed devices, the photocurrent density (J_{ph}) as a function of effective voltage (V_{eff}) (Figure 6f; Figures S14,S15, Supporting Information) was measured with function $J_{ph} = J_L - J_D$ (J_L and J_D represent the current densities under illumination and in the dark, respectively) and $V_{eff} = V_0 - V_{bias}$ (V_0 and V_{bias} represent the voltage when $J_{ph} = 0$ applied bias voltage).[91] Under short-circuit conditions, the exciton dissociation efficiency (P_{diss}) was calculated using the function $P_{diss} = J_{ph}/J_{sat}$. When $V_{eff} = 2$ V, the carriers were rapidly collected at the electrodes, and J_{ph} reached saturation (J_{sat}). The P_{diss}/P_{coll} values are estimated to be 95.4%/72.3%, 96.0%/82.2%, and 92.5%/75.5% for the gravure-printed flexible devices processed from Tol, o-XY, and TMB, suggesting the exciton dissociation rate was similar but the charge collection efficiency was higher for the gravure-printed flexible devices processed from o-XY, which was also comparable to the spin-coated devices (Figure 6f; Figure S15, Supporting Information). Finally, the carrier dynamic of the printed devices processed from different solvents was studied through transient absorption spectra with 750 nm pump light selectively excite the BTP-BO-4Cl (Figures S16–S18, Supporting Information). The results indicated that the gravure-printed active layer processed from o-XY has faster exciton dissociation and a more sufficient long diffusion-mediated process before charge dissociation (Figure S19, Table S5, Supporting Information), which contributed to the highest photovoltaic performance.

We also fabricated devices at different printing speeds and drying time. The results showed the printing speed has a slight effect on the devices' performance, and similar PCE was achieved for devices with different printing speeds from 30–50 m min^{-1} (Figure S20, Supporting Information). Additionally, our results indicated that there is little difference in device efficiency between the drying time of 10 and 1 min, suggesting that the drying time for printed films can be controlled within 1 minute (Table S6, Supporting Information). Since during the industrial R2R printing, a faster hot air dying method will be used, therefore the drying time will be even shorter. This result indicates the drying issue in the rapid printing process can be resolved, suggesting the high feasibility of high-speed printing of the FOSCs in the future.

3. Conclusion

In summary, reducing the performance decrease during upscaling is a big challenge for the commercialization of FOSCs. To solve this problem, optimizing both the macroscopic and microstructure of printed films is important. In this work, we demonstrated that the solvent-dependent ink rheology behavior and phase separation dynamics during R2R printing were decisive for both of the two parts. The result revealed the ink rheological behavior, viscosity, and adhesion force greatly impacted the macroscopic quality of the film during printing. The evaporation rate of the solvents significantly impacted the aggregation rate of the acceptor molecular and influenced the domain sizes of the printed films. The gravure-printed active layer processed from o-XY exhibited a suitable phase-separation morphology, as well as good large-area homogeneity. Finally, the efficiency of the flexible large-area FOSCs with an area of 1 cm^2 reached 14.81%. Moreover, the efficiency of flexible modules with an active area of 28–104 cm^2 was higher than 13% with a high cell-to-module efficiency remaining ratio of ≈0.9. This work showed the impact of solvents on the rheology and phase separation dynamics during R2R printing, which would provide valuable insight for achieving high-efficiency large-area FOSCs modules.

Supporting Information

Supporting Information is available from the Wiley Online Library or from the author.

Acknowledgements

This work was supported by the National Natural Science Foundation of China (22475232, 62404239, 22135001), "Dual Carbon" Science and Technology Innovation of Jiangsu province (Industrial Prospect and Key Technology Research program) (BE2022021), Vacuum Interconnected Nanotech Workstation, Suzhou Institute of Nano-Tech and Nano-Bionics, Chinese Academy of Sciences (CAS).

Conflict of Interest

The authors declare no conflict of interest.

Data Availability Statement

The data that support the findings of this study are available from the corresponding author upon reasonable request.

Keywords

flexible organic solar cells, modules, phase separation, R2R printing, rheology properties

Received: January 3, 2025
Revised: March 6, 2025
Published online: March 17, 2025

---

[1] H. Yu, J. Wang, Q. Zhou, J. Qin, Y. Wang, X. Lu, P. Cheng, *Chem. Soc. Rev.* **2023**, *52*, 4132.
[2] G. Zhang, F. R. Lin, F. Qi, T. Heumüller, A. Distler, H.-J. Egelhaaf, N. Li, P. C. Y. Chow, C. J. Brabec, A. K. Y. Jen, H.-L. Yip, *Chem. Rev.* **2022**, *122*, 14180.
[3] D. Corzo, D. Rosas-Villalva, A. C., G. Tostado-Blázquez, E. B. Alexandre, L. H. Hernandez, J. Han, H. Xu, M. Babics, S. De Wolf, D. Baran, *Nat. Energy* **2023**, *8*, 62.
[4] K. Fukuda, K. Yu, T. Someya, *Adv. Energy Mater.* **2020**, *10*, 2000765.
[5] E. Ravishankar, M. Charles, Y. Xiong, R. Henry, J. Swift, J. Rech, J. Calero, S. Cho, R. E. Booth, T. Kim, A. H. Balzer, Y. Qin, C. Hoi Yi Ho, F. So, N. Stingelin, A. Amassian, C. Saravitz, W. You, H. Ade, H. Sederoff, B. T. O'Connor, *Cell Rep. Phys. Sci.* **2021**, *2*, 100381.
[6] D. Landerer, D. Bahro, H. Röhm, M. Koppitz, A. Mertens, F. Manger, F. Denk, M. Heidinger, T. Windmann, A. Colsmann, *Energy Technol.* **2017**, *5*, 1936.
[7] S. Berny, N. Blouin, A. Distler, H.-J. Egelhaaf, M. Krompiec, A. Lohr, O. R. Lozman, G. E. Morse, L. Nanson, A. Pron, T. Sauermann, N. Seidler, S. Tierney, P. Tiwana, M. Wagner, H. Wilson, *Adv. Sci.* **2016**, *3*, 1500342.
[8] W. Wang, S. Zhang, T. Zhang, C. Wang, Z. Chen, S. Cheng, Y. Xiao, J. Wang, Y. Cui, J. Hou, *Adv. Energy Mater.* **2024**, https://doi.org/10.1002/aenm.202404482.
[9] C. Wang, X. Ma, Y.-f. Shen, D. Deng, H. Zhang, T. Wang, J. Zhang, J. Li, R. Wang, L. Zhang, Q. Cheng, Z. Zhang, H. Zhou, C. Tian, Z. Wei, *Joule* **2023**, *7*, 2386.
[10] H. Li, J. Le, H. Tan, L. Hu, X. Li, K. Zhang, S. Zeng, Q. Liu, M. Zhang, L. Shi, Z. Cai, S. Liu, H. Li, L. Ye, X. Hu, Y. Chen, *Adv. Mater.* **2024**, *37*, 2411989.
[11] X. Lu, C. Xie, Y. Liu, H. Zheng, K. Feng, Z. Xiong, W. Wei, Y. Zhou, *Nat. Energy* **2024**, *9*, 793.
[12] B. Zhang, F. Yang, Y. Li, *Small Sci.* **2023**, *3*, 2300004.
[13] X. Meng, Z. Xing, X. Hu, Y. Chen, *Chin. J. Polym. Sci.* **2022**, *40*, 1522.
[14] E. Feng, C. Zhang, J. Chang, Y. Han, H. Li, Q. Luo, C.-Q. Ma, H.-L. Yip, L. Ding, J. Yang, *Cell Rep. Phys. Sci.* **2024**, *5*, 101883.
[15] A. Khasbaatar, Z. Xu, J.-H. Lee, G. Campillo-Alvarado, C. Hwang, B. N. Onusaitis, Y. Diao, *Chem. Rev.* **2023**, *123*, 8395.
[16] J. K. Lee, W. L. Ma, C. J. Brabec, J. Yuen, J. S. Moon, J. Y. Kim, K. Lee, G. C. Bazan, A. J. Heeger, *J. Am. Chem. Soc.* **2008**, *130*, 3619.
[17] T. Hao, W. Zhong, S. Leng, R. Zeng, M. Zhang, L. Zhu, Y. Yang, J. Song, J. Xu, G. Zhou, Y. Zou, Y. Zhang, F. Liu, *Sci. Chin. Chem.* **2022**, *65*, 1634.
[18] F. Zhao, C. Wang, X. Zhan, *Adv. Energy Mater.* **2018**, *8*, 1703147.
[19] Y. Shi, Y. Chang, K. Lu, Z. Chen, J. Zhang, Y. Yan, D. Qiu, Y. Liu, M. A. Adil, W. Ma, X. Hao, L. Zhu, Z. Wei, *Nat. Commun.* **2022**, *13*, 3256.
[20] C. Zhu, L. Meng, J. Zhang, S. Qin, W. Lai, B. Qiu, J. Yuan, Y. Wan, W. Huang, Y. Li, *Adv. Mater.* **2021**, *33*, 2100474.
[21] Z. Luo, Y. Gao, H. Lai, Y. Li, Z. Wu, Z. Chen, R. Sun, J. Ren, C. e. Zhang, F. He, H. Woo, J. Min, C. Yang, *Energy. Environ. Sci.* **2022**, *15*, 4601.
[22] W. Gao, R. Ma, T. A. Dela Peña, C. Yan, H. Li, M. Li, J. Wu, P. Cheng, C. Zhong, Z. Wei, A. K. Y. Jen, G. Li, *Nat. Commun.* **2024**, *15*, 1946.
[23] J. Song, C. Zhang, C. Li, J. Qiao, J. Yu, J. Gao, X. Wang, X. Hao, Z. Tang, G. Lu, R. Yang, H. Yan, Y. Sun, *Angew. Chem., Int. Ed.* **2024**, *63*, 202404297.
[24] M. Sun, Y. Xu, Z. Fu, L. Wang, M. Li, X.-T. Hao, X. Du, *Sol. RRL* **2024**, *8*, 2400102.
[25] T. Huang, S. Geng, D. Wang, Y. Zhang, N. Weng, X. Li, Q. Liao, Z. Zhang, J. Lu, J. Zhang, *Adv. Funct. Mater.* **2024**, *34*, 2315825.
[26] R. Ma, X. Jiang, J. Fu, T. Zhu, C. Yan, K. Wu, P. Müller-Buschbaum, G. Li, *Energy. Environ. Sci.* **2023**, *16*, 2316.
[27] C. Yang, M. Jiang, S. Wang, B. Zhang, P. Mao, H. Y. Woo, F. Zhang, J.-l. Wang, Q. An, *Adv. Mater.* **2024**, *36*, 2305356.
[28] G. Ji, W. Zhao, J. Wei, L. Yan, Y. Han, Q. Luo, S. Yang, J. Hou, C.-Q. Ma, *J. Mater. Chem. A* **2019**, *7*, 212.
[29] H. Li, S. Liu, X. Wu, Q. Qi, H. Zhang, X. Meng, X. Hu, L. Ye, Y. Chen, *Energy. Environ. Sci.* **2022**, *15*, 2130.
[30] Y. Liu, B. Liu, C.-Q. Ma, F. Huang, G. Feng, H. Chen, J. Hou, L. Yan, Q. Wei, Q. Luo, Q. Bao, W. Ma, W. Liu, W. Li, X. Wan, X. Hu, Y. Han, Y. Li, Y. Zhou, Y. Zou, Y. Chen, Y. Liu, L. Meng, Y. Li, Y. Chen, Z. Tang, Z. Hu, Z.-G. Zhang, Z. Bo, *Sci. Chin. Chem.* **2022**, *65*, 1457.
[31] Z. Wang, Y. Han, L. Yan, C. Gong, J. Kang, H. Zhang, X. Sun, L. Zhang, J. Lin, Q. Luo, C.-Q. Ma, *Adv. Funct. Mater.* **2021**, *31*, 2007276.
[32] Z. Wang, J. Guo, Y. Pan, J. Fang, C. Gong, L. Mo, Q. Luo, J. Lin, C. Ma, *Energy Environ. Mater.* **2024**, *7*, 12592.
[33] H. Jung, J. Kim, J. Park, M. Jahankhan, Y. Hwang, B. Kang, H. Kim, H.-Y. Park, P. Ahn, D. Um, J.-S. Jee, W. S. Shin, B. Kim, S.-H. Jin, C. E. Song, Y. Lee, *EcoMat* **2024**, *6*, 12421.
[34] L. Zhu, M. Zhang, G. Zhou, Z. Wang, W. Zhong, J. Zhuang, Z. Zhou, X. Gao, L. Kan, B. Hao, F. Han, R. Zeng, X. Xue, S. Xu, H. Jing, B. Xiao, H. Zhu, Y. Zhang, F. Liu, *Joule* **2024**, *8*, 3153.
[35] H.-C. Kwon, W. Jeong, Y.-S. Lee, J.-H. Jang, H.-S. Jeong, S. Kim, D. Song, A. Park, E. Noh, K. Lee, H. Kang, *Adv. Energy Mater.* **2022**, *12*, 2200023.
[36] P. Kopola, T. Aernouts, S. Guillerez, H. Jin, M. Tuomikoski, A. Maaninen, J. Hast, *Sol. Energy Mater. Sol. Cells* **2010**, *94*, 1673.
[37] J. Lee, A. Kim, S. M. Cho, H. Chae, *Korean J. Chem. Eng.* **2012**, *29*, 337.
[38] P. Kopola, T. Aernouts, R. Sliz, S. Guillerez, M. Ylikunnari, D. Cheyns, M. Välimäki, M. Tuomikoski, J. Hast, G. Jabbour, R. Myllylä, A. Maaninen, *Sol. Energy Mater. Sol. Cells* **2011**, *95*, 1344.
[39] M. M. Voigt, R. C. I. Mackenzie, S. P. King, C. P. Yau, P. Atienzar, J. Dane, P. E. Keivanidis, I. Zadrazil, D. D. C. Bradley, J. Nelson, *Sol. Energy Mater. Sol. Cells* **2012**, *105*, 77.
[40] C. Koidis, S. Logothetidis, S. Kassavetis, C. Kapnopoulos, P. G. Karagiannidis, D. Georgiou, A. Laskarakis, *Sol. Energy Mater. Sol. Cells* **2013**, *112*, 36.
[41] J. Yang, D. Vak, N. Clark, J. Subbiah, W. W. H. Wong, D. J. Jones, S. E. Watkins, G. Wilson, *Sol. Energy Mater. Sol. Cells* **2013**, *109*, 47.
[42] P. Apilo, J. Hiltunen, M. Välimäki, S. Heinilehto, R. Sliz, J. Hast, *Prog. Photovolt: Res. Appl.* **2015**, *23*, 918.
[43] M. Välimäki, P. Apilo, R. Po, E. Jansson, A. Bernardi, M. Ylikunnari, M. Vilkman, G. Corso, J. Puustinen, J. Tuominen, J. Hast, *Nanoscale* **2015**, *7*, 9570.
[44] Y. Lin, Y. Jin, S. Dong, W. Zheng, J. Yang, A. Liu, F. Liu, Y. Jiang, T. P. Russell, F. Zhang, F. Huang, L. Hou, *Adv. Energy Mater.* **2018**, *8*, 1701942.
[45] X. Meng, L. Zhang, Y. Xie, X. Hu, Z. Xing, Z. Huang, C. Liu, L. Tan, W. Zhou, Y. Sun, W. Ma, Y. Chen, *Adv. Mater.* **2019**, *31*, 1903649.
[46] G. Wang, J. Zhang, C. Yang, Y. Wang, Y. Xing, M. A. Adil, Y. Yang, L. Tian, M. Su, W. Shang, K. Lu, Z. Shuai, Z. Wei, *Adv. Mater.* **2020**, *32*, 2005153.
[47] Y.-F. Shen, H. Zhang, J. Zhang, C. Tian, Y. Shi, D. Qiu, Z. Zhang, K. Lu, Z. Wei, *Adv. Mater.* **2023**, *35*, 2209030.
[48] Y. W. Han, S. J. Jeon, H. S. Lee, H. Park, K. S. Kim, H.-W. Lee, D. K. Moon, *Adv. Energy Mater.* **2019**, *9*, 1902065.

[49] X. Gu, Y. Zhou, K. Gu, T. Kurosawa, Y. Guo, Y. Li, H. Lin, B. C. Schroeder, H. Yan, F. Molina-Lopez, C. J. Tassone, C. Wang, S. C. B. Mannsfeld, H. Yan, D. Zhao, M. F. Toney, Z. Bao, *Adv. Energy Mater.* **2017**, *7*, 1602742.
[50] Y.-C. Huang, H.-C. Cha, C.-Y. Chen, C.-S. Tsao, *Prog. Photovolt: Res. Appl.* **2017**, *25*, 928.
[51] L. Lucera, F. Machui, P. Kubis, H. D. Schmidt, J. Adams, S. Strohm, T. Ahmad, K. Forberich, H. J. Egelhaaf, C. J. Brabec, *Energy. Environ. Sci.* **2016**, *9*, 89.
[52] K. Zhang, Z. Chen, A. Armin, S. Dong, R. Xia, H.-L. Yip, S. Shoaee, F. Huang, Y. Cao, *Sol. RRL* **2018**, *2*, 1700169.
[53] C.-Y. Liao, Y. Chen, C.-C. Lee, G. Wang, N.-W. Teng, C.-H. Lee, W.-L. Li, Y.-K. Chen, C.-H. Li, H.-L. Ho, P. H.-S. Tan, B. Wang, Y.-C. Huang, R. M. Young, M. R. Wasielewski, T. J. Marks, Y.-M. Chang, A. Facchetti, *Joule* **2020**, *4*, 189.
[54] Y.-J. Liao, Y.-C. Hsieh, J.-T. Chen, L.-S. Yang, X.-Z. Jian, S.-H. Lin, Y.-R. Lin, L.-M. Chen, F. Li, Y.-T. Hsiao, C.-Y. Liao, Y.-M. Chang, Y.-Y. Huang, C.-S. Tsao, S.-F. Horng, Y.-C. Chao, H.-F. Meng, *ACS Appl. Mater. Interfaces* **2023**, *15*, 7911.
[55] S. Rasool, D. V. Vu, C. E. Song, H. K. Lee, S. K. Lee, J.-C. Lee, S.-J. Moon, W. S. Shin, *Adv. Energy Mater.* **2019**, *9*, 1900168.
[56] S.-H. Chen, C. H. Liao, C. Y. Chang, K. M. Huang, J. Y. Chen, C. H. Chen, H.-F. Meng, H.-W. Zan, S.-F. Horng, Y.-C. Lin, M.-H. Yeh, *Org. Electron.* **2019**, *75*, 105376.
[57] Z. Jia, J. Pan, X. Chen, Y. Li, T. Liu, H. Zhu, J. Yao, B. Yan, Y. Yang, *Energy. Environ. Sci.* **2024**, *17*, 3908.
[58] H. Chen, R. Zhang, X. Chen, G. Zeng, L. Kobera, S. Abbrent, B. Zhang, W. Chen, G. Xu, J. Oh, S.-H. Kang, S. Chen, C. Yang, J. Brus, J. Hou, F. Gao, Y. Li, Y. Li, *Nat. Energy* **2021**, *6*, 1045.
[59] S. Wang, L.-Y. Xu, B. Xiao, M. Chen, M. Zhang, W. Gao, B. Xiao, A. K. Y. Jen, R. Yang, J. Min, R. Sun, *Energy. Environ. Sci.* **2024**, *17*, 2610.
[60] R. Sun, Q. Wu, J. Guo, T. Wang, Y. Wu, B. Qiu, Z. Luo, W. Yang, Z. Hu, J. Guo, M. Shi, C. Yang, F. Huang, Y. Li, J. Min, *Joule* **2020**, *4*, 407.
[61] H. Wang, S. Liu, H. Li, M. Li, X. Wu, S. Zhang, L. Ye, X. Hu, Y. Chen, *Adv. Mater.* **2024**, *36*, 2313098.
[62] H. Chen, W. Sun, R. Zhang, Y. Huang, B. Zhang, G. Zeng, J. Ding, W. Chen, F. Gao, Y. Li, Y. Li, *Adv. Mater.* **2024**, *36*, 2402350.
[63] B. Zhang, W. Chen, H. Chen, G. Zeng, R. Zhang, H. Li, Y. Wang, X. Gu, W. Sun, H. Gu, F. Gao, Y. Li, Y. Li, *Energy. Environ. Sci.* **2024**, *17*, 2935.
[64] T. Gokulnath, H. Kim, D. Song, H.-Y. Park, J.-S. Jee, Y. Y. Kim, J. Yoon, K. Kranthiraja, S.-H. Jin, *EcoMat.* **2024**, *6*, 12496.
[65] T. Chen, X. Zheng, D. Wang, Y. Zhu, Y. Ouyang, J. Xue, M. Wang, S. Wang, W. Ma, C. Zhang, Z. Ma, S. Li, L. Zuo, H. Chen, *Adv. Mater.* **2024**, *36*, 2308061.
[66] G. Hernandez-Sosa, N. Bornemann, I. Ringle, M. Agari, E. Dörsam, N. Mechau, U. Lemmer, *Adv. Funct. Mater.* **2013**, *23*, 3164.
[67] S. M. Mousavi, S. Raveshiyan, Y. Amini, A. Zadhoush, *Adv. Colloid Interface Sci.* **2023**, *319*, 102986.
[68] A. Jukić, F. Faraguna, I. Franjić, S. Kuzmić, *J. Ind. Eng. Chem.* **2017**, *56*, 270.
[69] Y. Liu, K. Zhou, X. Zhou, W. Xue, Z. Bi, H. Wu, Z. Ma, W. Ma, *Macromol. Rapid Commun.* **2022**, *43*, 2100871.
[70] X. Xu, L. Yu, H. Yan, R. Li, Q. Peng, *Energy. Environ. Sci.* **2020**, *13*, 4381.
[71] A. J. B. Milne, A. Amirfazli, *Langmuir* **2009**, *25*, 14155.
[72] C. G. L. Furmidge, *J. Colloid Sci.* **1962**, *17*, 309.
[73] B. A. Collins, E. Gann, L. Guignard, X. He, C. R. McNeill, H. Ade, *J. Phys.Chem.Lett.* **2010**, *1*, 3160.
[74] S. Mukherjee, C. M. Proctor, G. C. Bazan, T.-Q. Nguyen, H. Ade, *Adv. Energy Mater.* **2015**, *5*, 1500877.
[75] L. Ye, B. A. Collins, X. Jiao, J. Zhao, H. Yan, H. Ade, *Adv. Energy Mater.* **2018**, *8*, 1703058.
[76] J. Fang, Z. Wang, Y. Chen, Q. Zhang, J. Zhang, L. Zhu, M. Zhang, Z. Cui, Z. Wei, H. Ade, C.-Q. Ma, *Cell Rep. Phys. Sci.* **2022**, *3*, 100983.
[77] Z. Chen, A. Lohr, C. R. Saha-Möller, F. Würthner, *Chem. Soc. Rev.* **2009**, *38*, 564.
[78] F. C. Spano, C. Silva, *Annu. Rev. Phys. Chem.* **2014**, *65*, 477.
[79] K. D. Rosenthal, M. P. Hughes, B. R. Luginbuhl, N. A. Ran, A. Karki, S.-J. Ko, H. Hu, M. Wang, H. Ade, T.-Q. Nguyen, *Adv. Energy Mater.* **2019**, *9*, 1901077.
[80] J. Liu, S. Shao, H. Wang, K. Zhao, L. Xue, X. Gao, Z. Xie, Y. Han, *Org. Electron.* **2010**, *11*, 775.
[81] M.-Y. Chiu, U.-S. Jeng, C.-H. Su, K. S. Liang, K.-H. Wei, *Adv. Mater.* **2008**, *20*, 2573.
[82] Y. Zhang, W. Deng, C. E. Petoukhoff, X. Xia, Y. Lang, H. Xia, H. Tang, H. T. Chandran, S. Mahadevan, K. Liu, P. W. K. Fong, Y. Luo, J. Wu, S.-W. Tsang, F. Laquai, H. Wu, X. Lu, Y. Yang, G. Li, *Joule* **2024**, *8*, 509.
[83] Y. Wang, X. Wang, B. Lin, Z. Bi, X. Zhou, H. B. Naveed, K. Zhou, H. Yan, Z. Tang, W. Ma, *Adv. Energy Mater.* **2020**, *10*, 2000826.
[84] L. Li, N. Li, J. Hai, S. Gao, H. Xu, M. Luo, X. Zhou, X. Shi, S. Xu, X. Li, Z. Lu, Y. Pang, M. Li, H. Xia, S. Chen, X. Song, *Chem. Eng. J.* **2025**, *503*, 158263.
[85] J. J. Michels, S. H. P. M. de Winter, L. H. G. Symonds, *Org. Electron.* **2009**, *10*, 1495.
[86] A. de la Fuente Vornbrock, D. Sung, H. Kang, R. Kitsomboonloha, V. Subramanian, *Org. Electron.* **2010**, *11*, 2037.
[87] K. Sheybani, M. H. Paydar, M. H. Shariat, N. Setoudeh, *J. Min. Metall. Sect. B Metall.* **2020**, *56*, 361.
[88] R. Yu, H. Yao, Y. Cui, L. Hong, C. He, J. Hou, *Adv. Mater.* **2019**, *31*, 1902302.
[89] Q. Liu, K. Vandewal, *Adv. Mater.* **2023**, *35*, 2302452.
[90] K. Chong, X. Xu, H. Meng, J. Xue, L. Yu, W. Ma, Q. Peng, *Adv. Mater.* **2022**, *34*, 2109516.
[91] N. Wei, J. Chen, Y. Cheng, Z. Bian, W. Liu, H. Song, Y. Guo, W. Zhang, Y. Liu, H. Lu, J. Zhou, Z. Bo, *Adv. Mater.* **2024**, *36*, 2408934.